

THE PERFORMANCE OF THE ROBO-AO LASER GUIDE STAR ADAPTIVE OPTICS SYSTEM AT THE KITT PEAK 2.1-M TELESCOPE

REBECCA JENSEN-CLEM¹, DMITRY A. DUEV¹, REED RIDDLE¹, MAÏSSA SALAMA², CHRISTOPH BARANEC², NICHOLAS M. LAW³, S. R. KULKARNI¹ & A. N. RAMPRAKASH⁴

¹Department of Astronomy, California Institute of Technology, 1200 E. California Blvd., Pasadena, CA 91101, USA

²Institute for Astronomy, University of Hawai'i at Mānoa, Hilo, HI 96720-2700, USA

³Department of Physics and Astronomy, University of North Carolina at Chapel Hill, Chapel Hill, NC 27599-3255, USA

⁴Inter-University Centre for Astronomy & Astrophysics, Savitribai Phule Pune University Campus, Pune 411 007, India

ABSTRACT

Robo-AO is an autonomous laser guide star adaptive optics system recently commissioned at the Kitt Peak 2.1-m telescope. Now operating every clear night, Robo-AO at the 2.1-m telescope is the first dedicated adaptive optics observatory. This paper presents the imaging performance of the adaptive optics system in its first eighteen months of operations. For a median seeing value of 1.31", the average Strehl ratio is 4% in the i' band and 29% in the J band. After post-processing, the contrast ratio under sub-arcsecond seeing for a $2 \leq i' \leq 16$ primary star is five and seven magnitudes at radial offsets of 0.5" and 1.0", respectively. The data processing and archiving pipelines run automatically at the end of each night. The first stage of the processing pipeline shifts and adds the data using techniques alternately optimized for stars with high and low SNRs. The second "high contrast" stage of the pipeline is eponymously well suited to finding faint stellar companions.

1. INTRODUCTION

Adaptive optics (AO) systems correct wavefront aberrations introduced by the atmosphere and instrumental optics, restoring the resolution of a telescope to the diffraction limit. Laser guide stars (LGS) were developed in the 1980s to provide AO systems with bright, locatable wavefront reference sources, bringing fainter astrophysical objects into the purview of adaptive optics. Over half of all >8-m aperture telescopes are now equipped with an LGS AO system. The primary application of these AO instruments is for high angular resolution studies of interesting astronomical objects. As such minimizing the overhead has not been a major consideration in the overall design of AO systems on large telescopes.

Robo-AO is a robotic LGS AO system designed for maximum target throughput. Unlike LGS systems on large telescopes, it is based on an artificial star produced by Rayleigh scattering of a near UV laser. Robo-AO achieves high target throughput by minimizing overhead times to less than one minute per target. This is accomplished by three key design elements: 1) each step of the observation sequence is automated, allowing tasks that would be performed sequentially by a human operator to be performed in parallel and with minimal delay by the robotic system; 2) the $\lambda = 355$ nm Rayleigh scattering laser guide star is invisible to the human eye. As a

result, while coordination with the U.S. Air Force Joint Space Operations Center (JSpOC) is still required to prevent illumination of sensitive space assets, no control measures are required by the Federal Aviation Administration; 3) Robo-AO employs an automated queue scheduler which chooses each new science target based on telescope slew times and approved lasing windows provided in advance by JSpOC.

Robo-AO was first commissioned at the Palomar 1.5-m telescope in 2011, where it completed 19 science runs as a PI instrument from May 2012 through June 2015. Full details of the Robo-AO hardware and software can be found in Baranec et al. (2013), Baranec et al. (2014) and Riddle et al. (2014).

In 2012, the National Optical Astronomy Observatory (NOAO), following the recommendation of the Portfolio Committee which was chartered by the the National Science Foundation (NSF), decided to divest the Kitt Peak 2.1-m telescope. In 2015, the Robo-AO team made a bid for the telescope and was selected to operate the telescope for three years. Robo-AO was installed at the 2.1-m telescope in November, 2015; since then it has been operating nearly every clear night. As the first dedicated, automated adaptive optics facility, Robo-AO at Kitt Peak is well positioned to support the next generation of large-scale survey programs that are focused on stellar and exoplanet astronomy (e.g. K2, GAIA, CRTS,

Telescope	Kitt Peak 2.1-m telescope
Science camera	Andor iXon DU-888
EMCCD detector	E2V CCD201-20
Read-noise (without EM gain)	$47 e^-$
EM gain, selectable	300, 200, 100, 50, 25
Effective read-noise	0.16, 0.24, 0.48, 0.96, $1.9 e^-$
Full-frame-transfer readout	8.6 frames per second
Detector format	1024^2 13- μm pixels
Field of view	$36'' \times 36''$
Pixel scale	35.1 milli-arcsec per pixel
Observing filters	$g', r', i', z', \text{lp600}$

Table 1. The specifications of the Robo-AO optical detector at Kitt Peak.

PTF, TESS and others), as well as AO follow up of interesting sources. Early science results including Robo-AO KP data can be found in [Adams et al. \(2017\)](#) and [Vanderburg et al. \(2016a,b\)](#).

In this paper, we describe the performance of Robo-AO since commissioning. The paper is organized as follows: §2 introduces the Robo-AO imaging systems; §3 provides an overview of our automatic data reduction pipelines; §4 shows the relationships between the weather conditions and the measured seeing; §5 presents the Strehl ratio and contrast curve statistics as well as the point spread function (PSF) morphology; §6 describes our automated data archiving system; finally, §7 describes the newly installed near-IR camera.

2. SUMMARY OF THE ROBO-AO IMAGING SYSTEM

The Robo-AO imaging system includes two optical relays, each using a pair of off-axis parabolic mirrors. The first relay images the telescope pupil onto a 140-actuator Boston Micromachines micro-electromechanical-systems (MEMS) deformable mirror used for wavefront correction. A dichroic then reflects the UV light to an 11×11 Shack-Hartmann wavefront sensor. The second optical relay includes a fast tip-tilt correcting mirror and an atmospheric dispersion corrector (ADC; here, two rotating prisms¹) located at a reimaged pupil. The output of the second relay is an F/41 beam that is intercepted by a dichroic mirror, which reflects the $\lambda < 950 \text{ nm}$ portion of the converging beam to the visible wavelength filter wheel and EMCCD detector (see Table 1). The filter wheel includes g', r', i' ,

and z' filters, as well as a long-pass “lp600” filter cutting on at 600 nm and extending beyond the red limit of the EMCCD (see Figure 1 in [Baranec et al. 2014](#)). The dichroic transmits the longer wavelength light to the near-infrared (NIR) instrument port (see §7).

Robo-AO was originally designed for simultaneous optical and NIR operations, such that deep science integrations could be obtained in one band while the image displacement could be measured in the other and corrected with the fast tip-tilt mirror. In February of 2017, we achieved first light with a science-grade novel infrared array, a brief summary of which appears in §7². In this paper, we consider the imaging performance of Robo-AO using the optical imaging camera only. In lieu of an active tip-tilt correction, the EMCCD is run at a frame rate of 8.6 Hz to allow for post-facto image registration followed by stacking (see §3).

3. DATA REDUCTION PIPELINES

3.1. Overview

Image registration and stacking (see §2) is accomplished automatically by the “bright star” and “faint star” pipelines, which are optimized for high and low signal-to-noise (SNR) targets, respectively. The data are then processed by the “high contrast” pipeline to maximize the sensitivity to faint companions. These pipelines are described in detail below.

3.2. Image Registration Pipelines

All observations are initially processed by the “bright star” pipeline. This pipeline generates a windowed datcube centered on an automatically selected guide star. The windowed region is bi-cubically up-sampled and cross correlated with the theoretical point spread function to give the center coordinates of the guide star’s PSF in each frame. The full-frame, unprocessed images are then calibrated using the nightly darks and dome flats. Finally, the calibrated full frames are aligned using the center coordinates identified by the up-sampled, windowed frames, and co-added via the Drizzle algorithm ([Fruchter & Hook 2002](#)). These steps are described in detail in [Law et al. \(2014\)](#).

After an observation has been processed by the “bright star” pipeline, the core of the brightest star in the frame is fit by a 2D Moffat function. If the full width at half maximum (FWHM) of the function fit to the core is $< \lambda/D$, indicating that the stellar centroiding step has failed, the observation is re-processed by the “faint star” pipeline to improve the SNR in the final science image.

¹ From the commissioning of Robo-AO at Kitt Peak in November of 2015 through February of 2017, the right ascension (RA) axis of the 2.1-m telescope suffered from a $\sim 3.7 \text{ Hz}$ jitter (see §5.1 and §A) that caused a slight elongation of the stellar PSFs. As a result, the ADCs were not correctly calibrated until an upgrade to the telescope control system removed the jitter.

² A detailed analysis of the operation of this camera, its imaging performance, and its incorporation into an active tip-tilt control loop will be reported elsewhere.

The individual frames for a given observation are summed to create a master, dark and flat corrected reference image. This frame is then high pass filtered and windowed about the guide star. Each raw short exposure frame is then dark and flat corrected, filtered, and windowed. These individual frames are registered to the master reference frame using the `Image Registration for Astronomy` python package written by Adam Ginsburg³. The package finds the offset between the individual and reference frames using DFT up-sampling and registers the images with FFT-based sub-pixel image shifts. Figure 1 illustrates the strengths and weaknesses of the bright and faint star pipelines.

These automatic pipelines have reduced thousands of Robo-AO observations since the instrument was commissioned in November of 2015. Figure 2 shows a collage of representative observations.

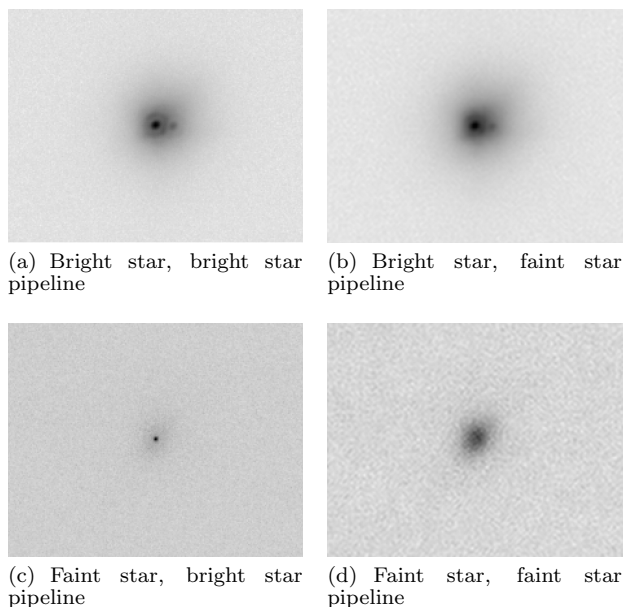


Figure 1. The bright star pipeline (a) produces a superior Strehl ratio for the $V= 8.84$ double star HIP55872 compared with (b) the faint star pipeline. For the $V= 15.9$ star 2MASSJ1701+2621, however, the bright star pipeline (c) fails to correctly center the PSF, leading to an erroneously bright pixel in the center. The faint pipeline (d) successfully shifts and adds this observation.

3.3. High Contrast Pipeline

For science programs that aim to identify point sources at small angular separations from known stars further processing is needed. Our “high contrast imaging” pipeline generates a $3.5''$ frame windowed about the star of interest in the final science frame. A high

pass filter is applied to the windowed frame to reduce the contribution of the stellar halo. To whiten correlated speckle noise at small angular separations from the target star we subtract a synthetic PSF generated by Karhunen-Loève Image Processing (KLIP). The KLIP algorithm is based on the method of Principal Component Analysis (Soummer et al. 2012). The PSF diversity needed to create this synthetic image is provided by a reference library of Robo-AO observations – a technique called Reference star Differential Imaging (RDI; Lafrenire et al. 2009). We note that the angular differential imaging approach (Marois et al. 2006) is not possible here because the 2.1-m telescope is an equatorial mount telescope. Our pipeline uses the `Vortex Image Processing` (VIP) package (Gomez Gonzalez et al. 2016).

The full reference PSF library consists of several thousand $3.5''$ square high pass filtered frames that have been visually vetted to reject fields with more than one point source. The PSF library is updated on a nightly basis to ensure that each object’s reduction has the opportunity to include frames from the same night. Each frame in the full library is cross correlated with the windowed and filtered science frame of interest. The five frames with the highest cross correlation form the sub-library provided to KLIP. We then adopt only the first principal component (PC) as our synthetic PSF, as including more PCs provides no additional noise reduction on average. A future version of the pipeline will choose the number of PCs automatically for each observation based on SNR maximization.

Figure 3 shows an example of a PSF reduced by the standard data pipeline (panel a), then high pass filtered (panel b), and finally processed with RDI-KLIP (panel c). After a science frame has been fully reduced we use VIP to produce a contrast curve that is properly corrected for small sample statistics and algorithmic throughput losses. The corresponding contrast curves for the three panels are shown in panel d.

Given that over two hundred new targets are observed during a clear night of Robo-AO observations the reference library is rapidly expanding and increasingly includes PSFs affected by a very wide range of environmental conditions. Hence, speckle noise in a past observation can be further reduced by a fresh RDI-KLIP reduction if the data is more correlated with later PSFs. Clearly a new reduction will benefit from the advantage of the larger reference library.

³ https://github.com/keflavich/image_registration

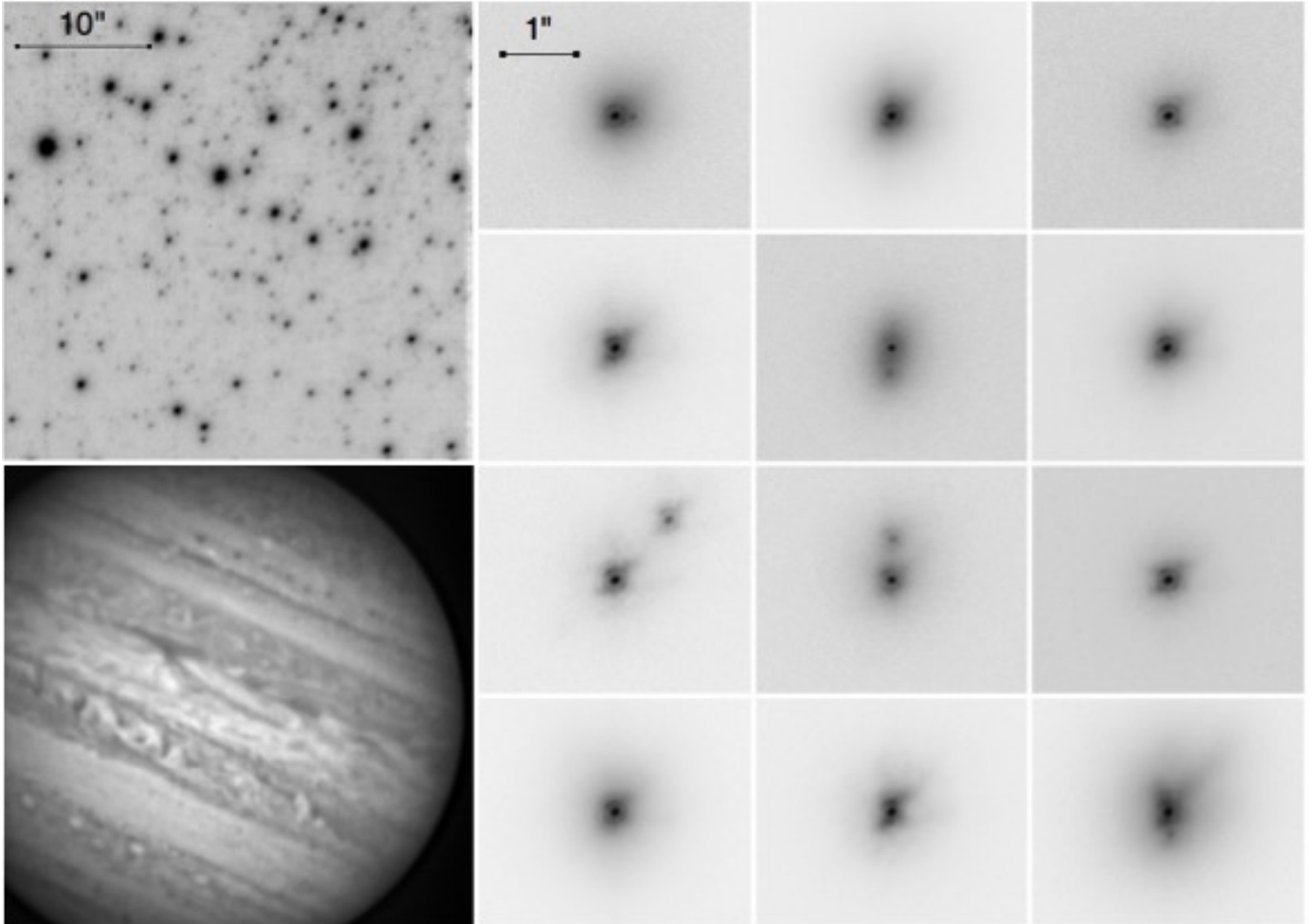
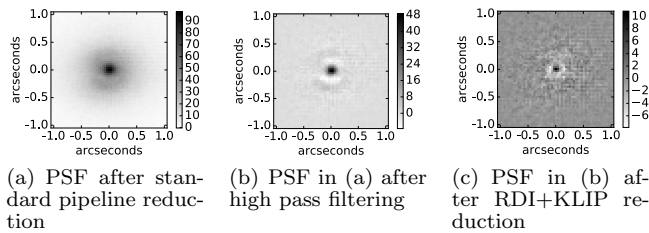
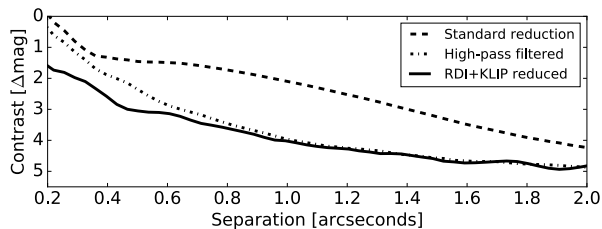


Figure 2. Examples of Robo-AO i' -band images at Kitt Peak (square root scaling) The full-frame ($36'' \times 36''$) images on the left are the globular cluster Messier 5 (top) and Jupiter (bottom). The images on the right are examples of bright single stars and stellar binaries with a range of separations and contrasts.



(a) PSF after standard pipeline reduction (b) PSF in (a) after high pass filtering (c) PSF in (b) after RDI+KLIP reduction



(d) The dashed, dot-dashed, and solid contrast curves correspond to the PSFs shown in (a), (b), and (c), respectively.

Figure 3. An example of the reduction steps in the “high contrast” pipeline for a z' observation of the star EPIC228859428.

4. SITE PERFORMANCE

4.1. Site Geography

Kitt Peak is located 56 miles southwest of Tucson, Arizona, at an elevation of 6800 feet. The 2.1-m telescope is situated 0.4 miles to the south of the peak’s highest point (the location of the Mayall 4-m telescope). The WIYN 3.5-m and 0.9-m telescopes are respectively 700 ft and 400 ft to the west of the 2.1-m telescope and at approximately the same elevation. There are no structures at equal or greater elevations to the east of the telescope, and the terrain is relatively flat beyond Kitt Peak in that direction. The 7730 ft Baboquivari Peak is 12 miles directly south of the telescope.

4.2. Seeing Measurement

Before the start of each science observation, a 10 s seeing observation is taken with the AO correction off. During this period the wavefront sensor camera acquires a background image. These seeing observations are dark and flat calibrated and summed without any registra-

tion of the individual exposures. The seeing is defined as the FWHM of a two-dimensional Gaussian function fit to this summed frame. Starting in January of 2017, a 90 s seeing observation was obtained each hour. Specifically, the Robo-AO queue schedules an observation of a bright ($V < 8$) star within 10° of zenith to refocus the telescope and measure the seeing. As of this writing, there is no significant difference between these “long” and “short” seeing observations. Here on we proceed with the assumption that the 10 s seeing measurements are representative of the long-exposure seeing.

We display a histogram of these fiducial seeing values in Figure 5. Figure 4 displays the seeing as a function of the seasons. The seeing values measured in a given wavelength are scaled to a fiducial wavelength of 500 nm by the scaling law $\text{seeing}_{500\text{ nm}} = \text{seeing}_\lambda \times (\lambda/500\text{ nm})^{1/5}$.

4.3. Seeing Contributions

We note that our median seeing of $1.31''$ differs from the median seeing of $0.8''$ reported by the adjacent WIYN telescope⁴. One possible explanation for this discrepancy is that the WIYN was built in 1994 with careful attention paid to dome ventilation and telescope thermal inertia. In contrast, the 2.1-m telescope saw first light in 1964 before such considerations were fully appreciated. Figure 6 demonstrates the challenging thermal conditions at the 2.1-m telescope: during the majority of Robo-AO observations, the mirror is warmer than the ambient dome temperature which in turn is warmer than the outside air. The experience of other observatories indicate that improvements to dome thermalization can significantly improve the measured seeing (e.g. Bauman et al. 2014).

Another possible cause of the comparatively poor seeing at the 2.1-m telescope is perhaps a more turbulent ground layer. Figure 7 shows a “wind rose,” or the frequency of wind speeds originating from different directions, for December 2015 through June 2016. We find that during this period the wind most commonly blows from the NNW, or the direction of the higher elevation Mayall 4-m telescope, and rarely from the SE where the terrain is less mountainous. The highest winds (> 40 mph) come from the north while the south has the largest fraction of low wind speeds (the wind speeds originating from within 20° of due south are under 10 mph 73% of the time).

Despite these terrain variations, the seeing is not significantly correlated with the wind direction. The wind speed, however, degrades the seeing by several tenths of an arcsecond for winds over 20 mph (the dome closes for winds over 40 mph).

Figure 8 plots the seeing versus the wind speed, demonstrating that poorer seeing is correlated with higher wind speeds⁵. We note that the wind monitor became nonfunctional after June of 2016, and hence further study of the relationship between the seeing and the wind speed will occur after a new wind monitor is in place.

5. ADAPTIVE OPTICS PERFORMANCE

5.1. Strehl Ratio

The goal of an adaptive optics system is to bring the observed PSF closer to its theoretical diffraction-limited shape; hence, an important measure of the AO system’s performance is the ratio between the peak intensity of an observed PSF and that of the telescope’s theoretical PSF – the Strehl ratio. As the AO performance improves, the Strehl ratio increases.

We calculate the Strehl ratio by 1) generating a monochromatic diffraction-limited PSF by Fourier transforming an oversampled image of the pupil, 2) combining several monochromatic PSFs to create a PSF representative of the desired bandpass, 3) re-sampling the polychromatic PSF to match our $0.0175''/\text{pixel}$ platescale of the up-sampled “drizzled” frames, 4) obtaining the “Strehl factor,” or the ratio of the peak intensity to the sum of the intensity in a $3''$ square box, and 5) calculating the Strehl ratio by repeating step 4 for the observed image and dividing by the Strehl factor. These steps are described in detail in Salama et al. (2016).

Once Robo-AO began regular observations at the 2.1-m telescope, we noticed that the achieved Strehl ratios were noticeably smaller than those that were achieved (for similar seeing values) at the Palomar 1.5-m telescope. A number of exercises were undertaken to determine possible causes for this degradation. Eventually, we determined that the Telescope Control System (TCS) was the main contributing factor. In Appendix A we discuss the problem in detail. The mitigation consisted of upgrading the TCS (completed February 2017). Below, and for the rest of the paper, we discuss the instrument performance since the TCS upgrade.

Figure 9 plots the Strehl ratio versus the measured seeing for the i' and lp600 filters. It is clear that the delivered Strehl ratio drops off quickly as the seeing increases – while Robo-AO achieves $> 10\%$ Strehl ratio when the seeing is $< 1.0''$, a $0.25''$ seeing increase halves the Strehl ratio.

⁵ The mean binned seeing measurements in Figure 8 are larger than the median of all Robo-AO KP seeing measurements (Figure 5) due to binning effects and the difference between the mean and median of the asymmetric distribution of seeing measurements.

⁴ <https://www.noao.edu/wiyn/aowiyn/>

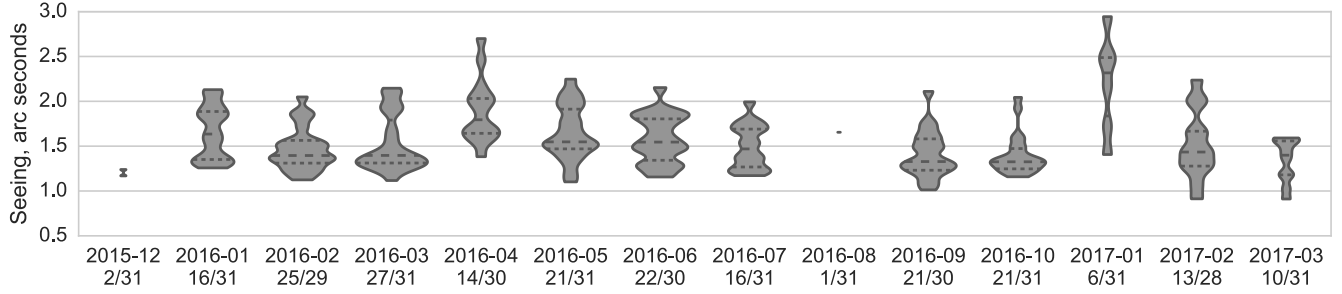


Figure 4. Seasonal fiducial ($\lambda = 500$ nm; see §4.2) seeing measurements. Nightly median values were used to fit a monthly distribution. The fraction of nights with seeing data for each month is shown. The quartile values and the actual measured range are shown.

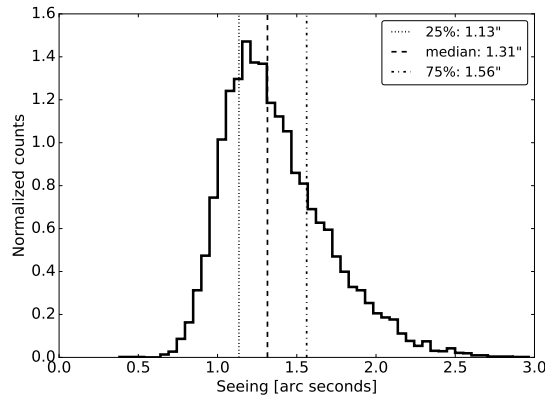


Figure 5. A histogram of the seeing measurements (all referenced to a wavelength $\lambda = 500$ nm) from December 2015 to March 2017. A zenith distance dependent correction has been applied. The 25th, 50th, and 75th percentile seeing values are indicated by the vertical lines.

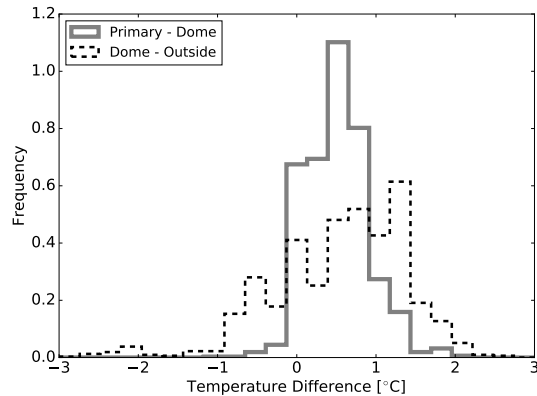


Figure 6. Histograms of the difference between the primary mirror and dome temperatures (solid) and the dome temperature minus the outside air temperature (dashed).

In Table 2 we present a detailed error budget under different seeing conditions. This error budget was originally developed by R. Dekany (private communication), and was validated against the on-sky performance of laser AO systems on the Keck telescope, the Hale tele-

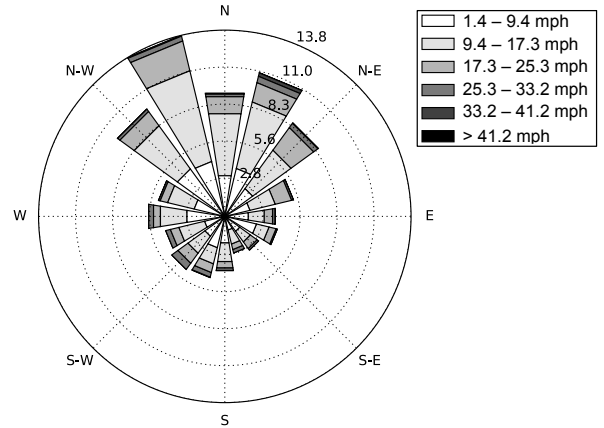


Figure 7. A “wind rose” showing a stacked polar histogram of wind speeds and directions from December 2015 through June 2016. The wind most frequently blows from the NW, N, and NE, which correspond to the more mountainous region towards the direction of the Mayall 4-m telescope. These also tend to be the direction of the high wind speeds while slower wind speeds most often come from the south, where the terrain is less mountainous.

scope and the Palomar 1.5-m telescope (Baranec et al. 2012). Since we lacked turbulence profile(s) for the 2.1-m telescope site we adopt a mean $C_n^2(h)$ profile from a MASS-DIMM atmospheric turbulence monitor collected over a year’s baseline at Palomar and scaled to the seeing at Kitt Peak.

High-order errors are added in quadrature and are dominated by Focal Anisoplanatism (which is an error arising from the finite altitude of the Rayleigh laser guide star resulting in imperfect atmospheric sampling). We estimate one-axis tip-tilt errors as being dominated by bandwidth error for magnitudes greater than 13. As noted in §2 we did not use the built-in tip-tilt facility but instead resorted to shift and add. We approximate the error resulting from this approach as follows. We assume a standard -3 db rejection frequency matching the full-frame rate of the science camera to approximate bandwidth error. The tip-tilt errors are then converted to an equivalent wavefront error and summed in quadra-

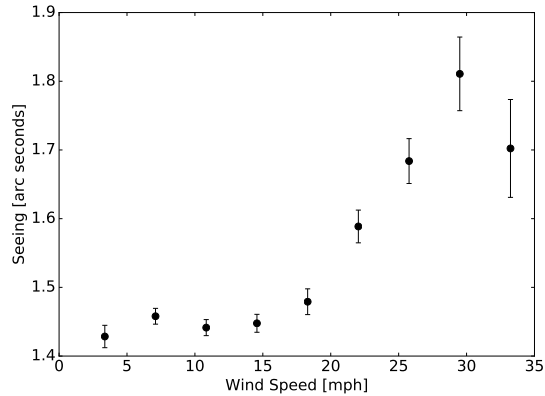


Figure 8. The mean binned seeing versus the wind speed for December 2015 through June 2016. The error bars are the standard deviation of the seeing values in a given wind speed bin divided by the square root of the number of seeing measurements in the bin. For wind speeds over 20 mph, the seeing is degraded by up to $0.3''$.

ture with the high-order errors. Other high-order and tip-tilt errors include chromatic, scintillation, aliasing, calibration and digitization errors.

Strehl ratios are calculated using the Maréchal approximation. The full-widths at half-maximum (FWHM) are calculated from PSF models assuming the residual diffraction-limited, concentrated light, residual seeing, and scattered light halos are proportional to the phase variance of the residual errors. These models have shown accuracy of a few percent for Strehl ratios as low as 4% (Sheehy et al. 2006). Figure 9 demonstrates Robo-AO’s ability to approach the predicted Strehl ratio of 14% in sub-arcsecond seeing conditions.

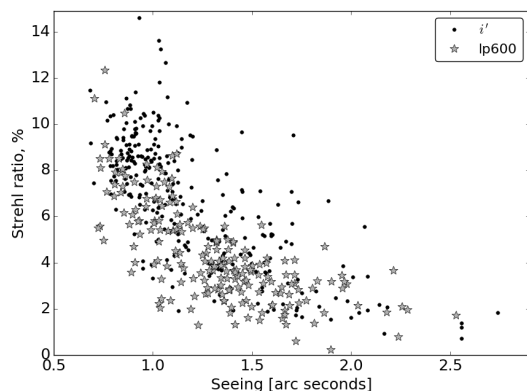


Figure 9. The Strehl ratio versus the measured seeing values for 21 February 2017 through 10 March 2017 in the i' and lp600 filters.

5.2. PSF Morphology

Figure 10 shows a representative Robo-AO point spread function (PSF) corresponding to the V=10 star

HIP56051. The observation was taken in the i' band with a total exposure time of 90s. The seeing at the time of the observation was $0.94''$, and the Strehl ratio of the final PSF is 10.17%.

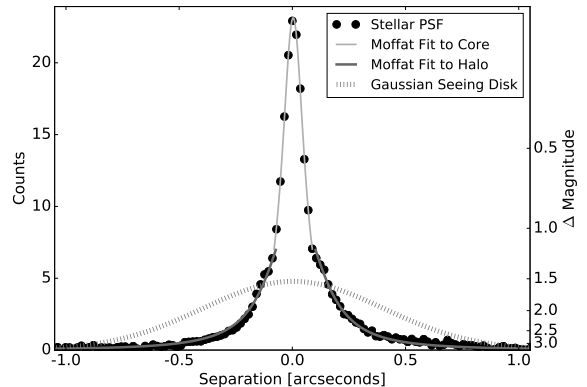


Figure 10. A 1D cut through the PSF of HIP56051 is plotted with two Moffat functions fit to the PSF core and halo, respectively. The dashed curve is a Gaussian distribution with a FWHM corresponding to the seeing measurement and an area equal to the observed PSF’s area.

The effect of the AO system is to re-arrange the starlight from the equivalent area seeing-limited PSF (dashed curve) to the sharper, observed PSF plotted by the black points. The AO-corrected PSF includes two components: a sharp core and a broader halo, each separately fit by Moffat functions (the light and dark gray curves, respectively). The full width at half maximum (FWHM) of the Moffat function fit to the core is $0.1'' \pm 0.01''$. This value is consistent with the diffraction limit of $1.028 \lambda/D = 0.08''$.

5.3. Contrast Curves

Section §3 described the “high contrast pipeline,” which produces 5σ contrast curves from the high pass filtered, RDI-PCA reduced science frames. Figure 11 plots the median and best 10% contrast curves for i' and lp600 filter science frames. Under sub-arcsecond seeing (the best 10% of cases), the contrast ratio for a $2 \leq i' \leq 16$ primary star is five and seven magnitudes at $0.5''$ and $1.0''$, respectively.

6. DATA ARCHIVE

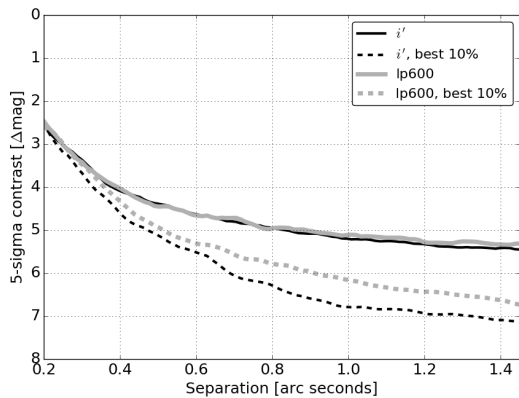
We have developed a fully automated data processing and archiving system⁶. The data reduction chain for an observing night proceeds as follows. At the end of each night, the visual camera data are compressed and transferred to the network storage. Next, the darks and dome

⁶ <https://github.com/dmitryduev/roboao-archive>

Table 2. The Robo-AO Error Budget

Percentile Seeing		25%	50%	75%
Seeing at Zenith	1.00''	1.13''	1.31''	1.56''
Zenith Angle	20	20	20	20
Effective Seeing	1.04''	1.17''	1.36''	1.62''
High-order Errors				
Atmospheric Fitting Error	65	72	82	95
Bandwidth Error	54	60	67	78
High-order Measurement Error	35	38	44	52
LGS Focal Anisoplanatism Error	99	109	124	143
Other High Order Errors	64	65	68	72
Total High Order Wavefront Error	149 nm	163 nm	182 nm	208 nm
Tip-Tilt Errors				
Tilt Bandwidth Error	24 mas	26 mas	30 mas	34 mas
Other Tip-Tilt Errors	7 mas	7 mas	7 mas	8 mas
Total Tip/Tilt Error (one-axis)	25 mas	27 mas	31 mas	35 mas
Total Effective Wavefront Error	165 nm	180 nm	200 nm	228 nm

Spectral Band	λ	λ/D	Strehl	FWHM	Strehl	FWHM	Strehl	FWHM	Strehl	FWHM
r'	0.62μ	$0.07''$	6%	$0.10''$	4%	$0.11''$	2%	$0.14''$	0%	$0.34''$
i'	0.75μ	$0.08''$	14%	$0.11''$	10%	$0.11''$	6%	$0.12''$	2%	$0.15''$
z'	0.88μ	$0.10''$	25%	$0.12''$	19%	$0.12''$	13%	$0.13''$	7%	$0.14''$
J	1.25μ	$0.14''$	49%	$0.15''$	43%	$0.16''$	35%	$0.16''$	26%	$0.17''$
H	1.64μ	$0.18''$	66%	$0.19''$	61%	$0.20''$	54%	$0.20''$	45%	$0.20''$

**Figure 11.** The contrast as a function of distance from the central star for the i' and lp600 filters. The dashed lines show the best 10% contrast curves for each filter.

flats taken at the beginning of each night are combined into master calibration files and applied to the observations. The bright star pipeline is then run on each observation followed by the computation of the Strehl ratio of the resulting image. The high contrast pipeline

also produces high pass filtered, PSF-subtracted images and contrast curves for each of these processed images (see Section 3). If the “drizzled” image produced by the bright star pipeline does not pass a quality check (i.e. if a 2-component Moffat fit to the PSF has an anomalously narrow core or wide halo) then the faint star pipeline re-reduces the rapid read-out data. Additionally, the “archiver” processes the nightly seeing data, and generates summary plots of the seeing measurements, Strehl ratios, and contrast curves. Completing the full reduction chain for a typical night’s worth of data takes a few hours.

The “house-keeping” system uses a Redis⁷-based huey python package⁸ to manage the processing queue, which distributes the jobs to utilize all available computational resources. The processing results together with ancillary information on individual observations and

⁷ An efficient in-memory key-value database

⁸ <https://github.com/coleifer/huey>

system performance are stored in a MongoDB⁹ NoSQL database. For interactive data access, we developed a web-based interface powered by the Flask¹⁰ back-end. It allows the user to access previews of the processing results together with auxiliary data (e.g. external VO images of a field), nightly summary and system performance information. The web application serves as the general interface to the database providing a sophisticated query interface and also has a number of analysis tools.

7. NEAR-INFRARED CAMERA

In November 2016, we installed a NIR camera for use with Robo-AO. While similar to the camera deployed in engineering tests at the Palomar 1.5-m telescope in 2014 (Baranec et al. 2015), the new camera uses a science-grade detector and faster readout electronics. The detector is a Mark 13 Selex ES Advanced Photodiode for High-speed Infrared Array (SAPHIRA) with an ME-911 Readout Integrated Circuit (Atkinson et al. 2016; Baker et al. 2016). It has sub-electron readnoise and 320×256-pixel array with $\lambda = 2.5 \mu\text{m}$ cutoff. The single-board PB1 ‘PizzaBox’ readout electronics were developed at the Institute for Astronomy and we use 32 readout channels, each capable of a 2 Mpixel/sec sampling rate, for a maximum full-frame read rate of $\sim 800\text{Hz}$.

The NIR camera attaches to the Robo-AO $f/41$ infrared camera port that accesses $\lambda > 950\text{nm}$ after transmission through a dichroic. The camera has an internal cold $\lambda < 1.85 \mu\text{m}$ short-pass filter and an external warm filter wheel with J, H, clear, and blocking filters. The camera has a plate scale of $0.064''$ per pixel and field-of-view of $16.5'' \times 20.6''$.

We achieved first light on sky in February 2017 during final testing of the upgraded TCS. Initially we used a 1 Mpixel/sec sampling rate (a full frame read rate of 390 Hz) with detector resets every 300 reads. To create a reduced image, we first assembled difference frames between 39 consecutive reads, totaling $\sim 0.1\text{s}$ of integration time, short enough to effectively freeze stellar image displacement. We subtracted a frame median to approximate removing the background. We then synthesized a long exposure image by registering each corrected frame on the brightest target in the field. Figure 12 shows an example image of a binary star observed in H-band.

For the moment, data acquisition and reduction is performed manually. In the coming months, we will optimize the detector readout routines for maximum sensitivity to faint objects (including dithering for background removal), integrate the operation of the camera



Figure 12. A 5.5 s image of GJ1116 taken in H-band with the near-infrared camera (linear stretch).

into the robotic queue and modify our existing data reduction pipeline to handle the NIR data. We will also investigate automating active tip-tilt correction by using either the visible or infrared camera as a tip-tilt camera, as previously demonstrated at Palomar.

8. CONCLUSION

Robo-AO at the Kitt Peak 2.1-m telescope is the first dedicated adaptive optics observatory. Observing every clear night, Robo-AO has the capacity to undertake LGS AO surveys of large samples. For instance, a 1000-star survey with exposure times of 60 s per target can be completed on the timescale of a week.

Science programs designed to exploit Robo-AO’s unique capabilities are underway. These programs include stellar multiplicity in open clusters, minor planet binarity, major planet weather variability, extragalactic object morphology, sub-stellar companions to nearby young stars, M-star multiplicity, and the influence of stellar companions on asteroseismology. By the summer of 2017, Robo-AO will become the first LGS AO system to operate entirely autonomously, as on-going upgrades to the 2.1-m telescope will remove the need for a human observer.

The Robo-AO team thanks NSF and NOAO for making the Kitt Peak 2.1-m telescope available. We thank the observatory staff at Kitt Peak for their efforts to assist Robo-AO KP operations. Robo-AO KP is a partnership between the California Institute of Technology, the University of Hawai’i, the University of North Carolina at Chapel Hill, the Inter-University Centre for Astronomy and Astrophysics (IUCAA) at Pune, India, and the National Central University, Taiwan. The Murty family feels very happy to have added a small value to this important project. Robo-AO KP is also supported by grants from the John Templeton Foundation and the Mt. Cuba Astronomical Foundation. The Robo-AO instrument was developed with support from the Na-

⁹ <https://www.mongodb.com>

¹⁰ <https://github.com/pallets/flask>

tional Science Foundation under grants AST-0906060, AST-0960343, and AST-1207891, IUCAA, the Mt. Cuba Astronomical Foundation, and by a gift from Samuel Oschin. These data are based on observations at Kitt Peak National Observatory, National Optical Astronomy Observatory (NOAO Prop. ID: 15B-3001), which

is operated by the Association of Universities for Research in Astronomy (AURA) under cooperative agreement with the National Science Foundation. C.B. acknowledges support from the Alfred P. Sloan Foundation.

Facility: KPNO:2.1m (Robo-AO)

REFERENCES

- Adams, E. R., Jackson, B., Endl, M., et al. 2017, *The Astronomical Journal*, 153, 82
- Atkinson, D. E., Hall, D. N. B., Baker, I. M., et al. 2016, in *Proc. SPIE*, Vol. 9915, *Society of Photo-Optical Instrumentation Engineers (SPIE) Conference Series*, 99150N
- Baker, I., Maxey, C., Hipwood, L., & Barnes, K. 2016, in *Proc. SPIE*, Vol. 9915, *Society of Photo-Optical Instrumentation Engineers (SPIE) Conference Series*, 991505
- Baranec, C., Atkinson, D., Riddle, R., et al. 2015, *The Astrophysical Journal*, 809, 70
- Baranec, C., Riddle, R., Ramaprakash, A. N., et al. 2012, in *Proc. SPIE*, Vol. 8447, *Adaptive Optics Systems III*, 844704
- Baranec, C., Riddle, R., Law, N. M., et al. 2013, *Journal of Visualized Experiments*
- . 2014, *The Astrophysical Journal Letters*, 790, L8
- Bauman, S. E., Benedict, T., Baril, M., et al. 2014, in *Proc. SPIE*, Vol. 9149, *Observatory Operations: Strategies, Processes, and Systems V*, 91491K
- Fruchter, A. S., & Hook, R. N. 2002, *Publications of the Astronomical Society of the Pacific*, 114, 144
- Gomez Gonzalez, C. A., Absil, O., Absil, P.-A., et al. 2016, *Astronomy and Astrophysics*, 589, A54
- Hardy, J. W. 1998, *Adaptive Optics for Astronomical Telescopes*, Oxford Series in Optical and Imaging Sciences (Oxford, New York: Oxford University Press)
- Lafrenire, D., Marois, C., Doyon, R., & Barman, T. 2009, *The Astrophysical Journal Letters*, 694, L148
- Law, N. M., Baranec, C., & Riddle, R. L. 2014, in *Proc. SPIE*, Vol. 9148, *Adaptive Optics Systems IV*, 91480A
- Marois, C., Lafrenire, D., Doyon, R., Macintosh, B., & Nadeau, D. 2006, *The Astrophysical Journal*, 641, 556
- Riddle, R. L., Hogstrom, K., Papadopoulos, A., Baranec, C., & Law, N. M. 2014, in *Proc. SPIE*, Vol. 9152, *Software and Cyberinfrastructure for Astronomy III*, 91521E
- Salama, M., Baranec, C., Jensen-Clem, R., et al. 2016, in *Proc. SPIE*, Vol. 9909, *Society of Photo-Optical Instrumentation Engineers (SPIE) Conference Series*, 99091A
- Sheehy, C. D., McCrady, N., & Graham, J. R. 2006, *ApJ*, 647, 1517
- Soummer, R., Pueyo, L., & Larkin, J. 2012, *The Astrophysical Journal Letters*, 755, L28
- Vanderburg, A., Becker, J. C., Kristiansen, M. H., et al. 2016a, *The Astrophysical Journal Letters*, 827, L10
- Vanderburg, A., Bieryla, A., Duev, D. A., et al. 2016b, *The Astrophysical Journal Letters*, 829, L9

APPENDIX

A. TELESCOPE JITTER

After moving Robo-AO from the Palomar 1.5-m telescope to the Kitt Peak 2.1-m telescope, the median Strehl ratio across all wavelengths was initially reduced from 5.8% to 3.2%. The source of this degradation was a ~ 3.7 Hz vibration in the RA axis. Because Robo-AO mitigates tip/tilt by post facto shift and add rather than a real-time loop, and because its framerate is typically only 8.6 Hz, the targets were smeared in the RA direction. Figure A1 a and b show the power spectral densities of the mean subtracted RA centroid positions of targets observed at Kitt Peak and Palomar, respectively. The peak at ~ 3.7 Hz is clear in the Kitt Peak data, but is not present at Palomar. The RA-axis smearing for a single test observation is demonstrated in Figure A2.

The jitter was mitigated by two changes to the system. First, the KPNO staff noticed a ticking sound corresponding to each rotation of the telescope drive worm gear, which was solved by lubrication. This step reduced the height of, but did not eliminate, the PSD peak. Second, we took a test observation in which only sidereal tracking was enabled, and all fine computer guiding was turned off. The peak was absent in this test observation, leading us to conclude that the telescope control system (TCS) was giving erroneous commands that “kicked” the telescope’s position. The TCS was replaced in the winter of 2017 to allow the Robo-AO robotic system to fully control the telescope’s motion, eliminating the remaining RA jitter (Figure A3). Figure A4 shows a comparison of the Strehl ratios versus the seeing before and after the TCS upgrade.

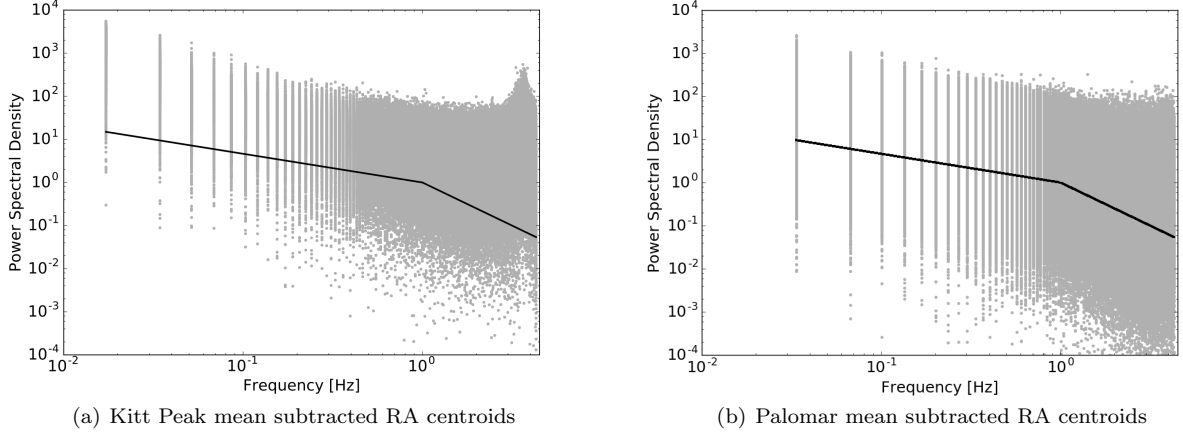


Figure A1. The power spectral densities of the mean subtracted RA target positions for each sub-exposure at Kitt Peak (a) and Palomar (b). The peak at ~ 3.7 Hz is present at Kitt Peak, but not at Palomar. The solid black lines show the theoretical power-law dependencies of the tilt: $f^{-2/3}$ at low frequencies, and f^{-2} for 1 – 10 Hz (Hardy 1998).

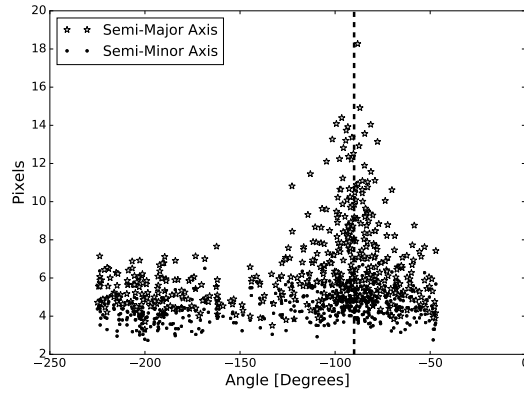


Figure A2. For a test observation, the standard deviation along the semi-major and semi-minor axes of 2D Gaussian fits to each 0.116s sub-exposure are plotted versus the rotation angle of the Gaussian. Here, -90° (dashed black line) indicates that the semi-major axis lies along the RA-axis. Clearly, the PSF is elongated along the RA-axis.

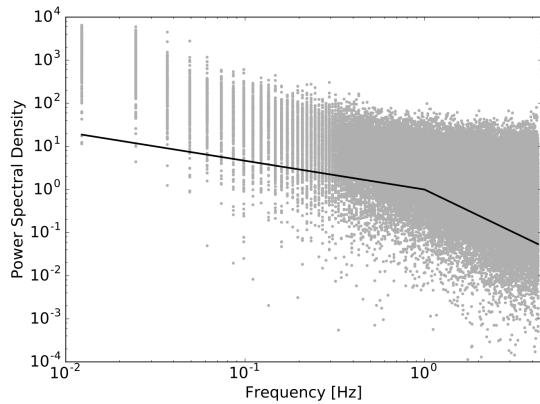


Figure A3. The power spectral densities of the mean subtracted RA target positions for the Kitt Peak sub-exposures since the telescope control upgrade (22 February 2017 through 8 March 2017). The peak that was present in Figure A1a is eliminated.

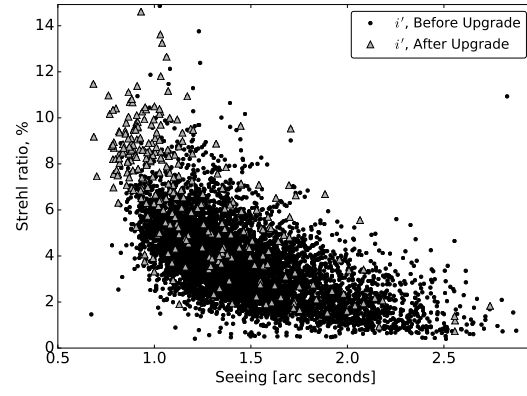


Figure A4. Strehl ratios of the observations taken in i' as a function of the seeing scaled to 500 nm before (December 2015 through 22 February 2017; black points) and after (22 February 2017 through 10 March 2017; gray stars) the enhancements. Note the significant improvement for seeing under ≈ 1.1 arcseconds.